Magnetoelectric coupling at metal surfaces

L. Gerhard[1], T. K. Yamada[1,2], T. Balashov[1], A. F. Takács[3], R. J. H. Wesselink[1], M. Däne[4,5], M. Fechner[4], S. Ostanin[4], A. Ernst[4], I. Mertig[4,6] and W. Wulfhekel[1]*

Magnetoelectric coupling allows the magnetic state of a material to be changed by an applied electric field. To date, this phenomenon has mainly been observed in insulating materials such as complex multiferroic oxides. Bulk metallic systems do not exhibit magnetoelectric coupling, because applied electric fields are screened by conduction electrons. We demonstrate strong magnetoelectric coupling at the surface of thin iron films using the electric field from a scanning tunnelling microscope, and are able to write, store and read information to areas with sides of a few nanometres. Our work demonstrates that high-density, non-volatile information storage is possible in metals.

Magnetoelectric coupling (MEC) has the potential to influence the magnetic state of matter through the application of an electric field, and is mediated by subtle crystal structure changes induced by the electric field affecting the magnetic properties. Two realizations of MEC in insulators exist. In the first, single-phase multiferroics combine both electric and magnetic dipole moments in the same phase, but only display low ordering temperatures[1–3]. In the second, ferroelectric and ferromagnetic phases can be brought into close contact so that electric and magnetic dipoles couple via the interface, driven by elastic[4,5] or electronic[6,7] effects. In both approaches, the electric polarization (the position of the ions in the ferroelectric material with respect to one another) can be switched by an applied electric field. In metals, the electric field cannot penetrate deeply, prohibiting MEC in the bulk because the field is screened by a free electron charge near the surface[8]. This screening surface charge extends into the vacuum, forming a surface barrier, which is reflected in the work function. In the vicinity of the surface, however, the interaction of the surface barrier with an external electric field causes substantial displacements of free electrons[9]. Similarly to the electrons, the cores of the surface atoms are also displaced, but in the opposite direction, as has been observed for non-magnetic palladium[10]. In magnetic systems these structural relaxations can in turn influence the magnetic order. This suggests the possibility of finding MEC at the surfaces of magnetic metals. A scanning tunnelling microscope (STM) is an ideal tool with which to investigate this, as it can image surface structures and it is possible to use the electric field underneath the STM tip to induce magnetic phase transitions.

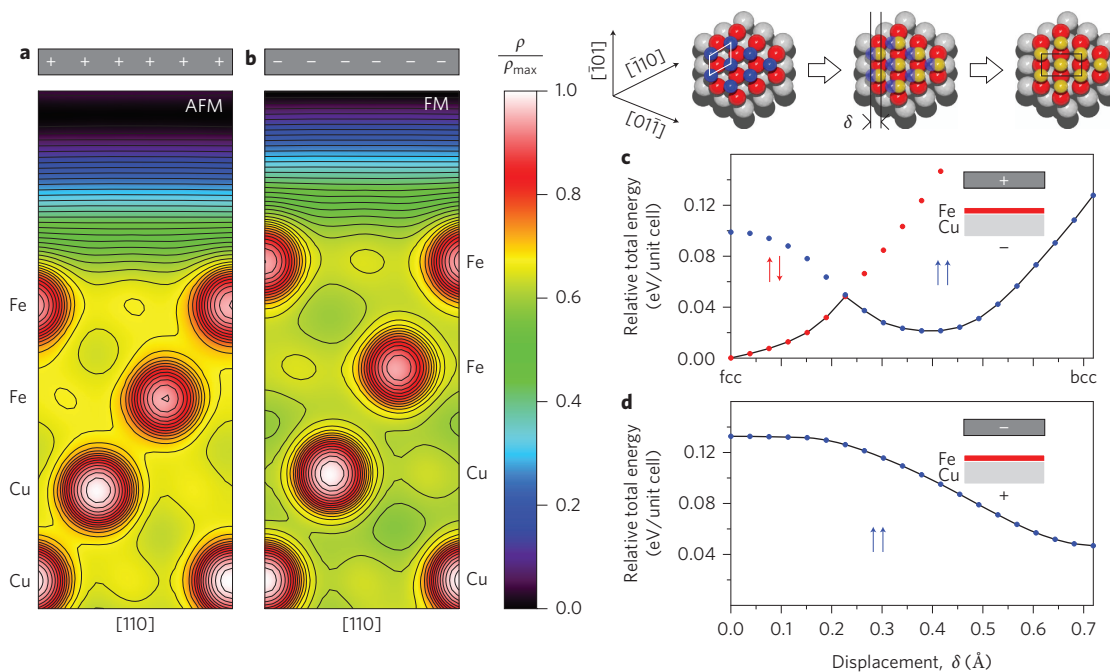## Computational design of magnetoelectric coupling

As a model system for surface MEC in metals, we used two atomic layers of Fe grown on Cu(111). Bulk Fe is known to have a structural instability between the face-centred cubic (fcc) and body-centred cube (bcc) phases, as well as a strong variation of the magnetic order following slight changes in the unit cell volume[11]. The phase transformation is caused by a diffusionless deformation of the lattice, termed the martensitic phase transition[12,13]. In this phase transition, the atomic volume of Fe is reduced when going from the bcc to the fcc phase, causing a change in the magnetic ground state. This behaviour is enhanced at the Fe surface and in

ultrathin Fe layers, which offers the opportunity to trigger structural and magnetic transitions by means of an external electric field interacting with the surface charge. Our calculations, performed for two atomic layers of Fe on Cu(111), predict that the crystal structure and therefore the magnetic order can be controlled by an electric field, allowing magnetic information to be written. Experimentally, the electric field was provided by an STM in the tunnelling regime. In response to the field, the Fe islands could be switched locally on the nanometre scale between the antiferromagnetic fcc and the ferromagnetic bcc configurations. These properties allow ultrathin Fe films to comprise a simple model system by using the interactions between magnetism, induced surface charge and elasticity.

First-principles calculations for the atomic relaxations of the bilayer Fe/Cu(111) surface under an applied electric field were performed with the Vienna *Ab Initio* Simulation Package (VASP)[14] using density functional theory. An applied electric field of $1 \times 10^9\ \mathrm{V\ m^{-1}}$ was used. The results of the simulations of field-induced vertical relaxations are presented in Fig. 1, showing the normalized total charge density distribution in the vicinity of the surface under the influence of positive (Fig. 1a) or negative (Fig. 1b) electrodes. As expected, the positively charged electrode repels the atoms towards the bulk, with a substantial reduction in the interlayer distances (Fig. 1a); however, the electron density at the surface is increased. With the negatively charged electrode (Fig. 1b), the iron atoms are attracted by the electrode and the electron density at the surface is reduced. Based on a total energy analysis we predict that Fe layers are layerwise antiferromagnetic in Fig. 1a and ferromagnetic in Fig. 1b. These findings are related to the remarkable magnetic phase properties of iron. In Fig. 1a, the interatomic distances are reduced which favours antiferromagnetic order, whereas in Fig. 1b, they are expanded, favouring ferromagnetic order in the system[11].

Because the electric field is perpendicular to the surface, the induced movements of the electrons and ion cores occur in the vertical direction. Vertical displacement is, however, not the only type of rearrangement that can take place in this system within a martensitic phase transition. According to a recent STM experiment, fcc and bcc phases coexist in Fe islands on the Cu(111) surface[15]. We therefore investigated possible fcc-to-bcc martensitic transitions

Figure 1 | Simulations of surface relaxations under the influence of an electric field in Fe/Cu(111). a,b, Normalized electronic charge density in fcc bilayers Fe and two underlying Cu layers under positive (**a**) and negative (**b**) electric fields. The electric field is modelled by a plate capacitor placed 4 Å above the surface. The electron charge is attracted (repelled) by the positively (negatively) charged electrode, causing the ions to move away from (towards) the surface. The Fe layers were found to be layerwise antiferromagnetic (AFM) in **a** and ferromagnetic (FM) in **b**. **c,d,** Relative total energy per unit cell as a function of the lateral displacement δ of the top Fe layer due to the martensitic phase transition (red for antiferromagnetic and blue for ferromagnetic states). When a positive electric field is applied, the iron atoms adopt fcc stacking, and the layer magnetizations align in an antiparallel arrangement (**c**). When the applied field is negative, bcc stacking of magnetic layers aligned in parallel is energetically preferred (**d**). The ball model illustrates the movement of the top Fe atoms from their threefold hollow site position of fcc (111) stacking (blue) to the bcc (110) bridge position (orange). Grey and red balls represent Cu and bottom Fe atoms, respectively. Lattice directions in the fcc (111) plane and respective unit cells are indicated.
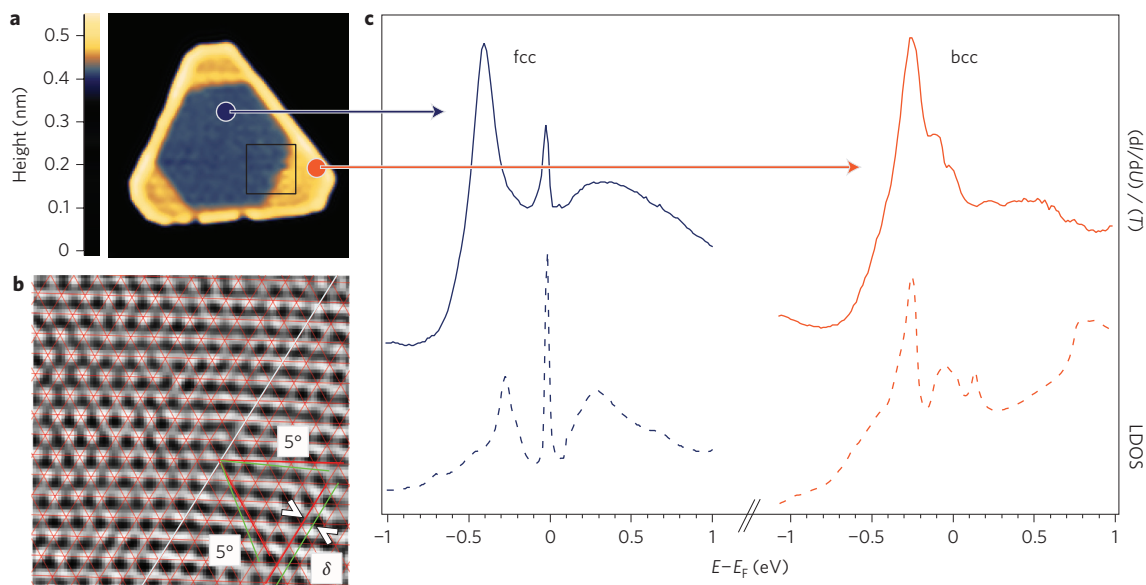
Figure 2 | Crystallographic and electronic structure of Fe islands. a, Topographic STM image showing two crystallographic phases in a bilayer Fe island on Cu(111) (image size, 19 nm × 19 nm). The coexisting phases can be distinguished by a difference in height. **b,** Atomically resolved image showing the fcc configuration on the left and the bcc configuration on the right. The top-layer atoms on the left follow the hexagonal fcc (111) structure of the Cu substrate (red grid). The atomic directions on the right (green line) show a slight misalignment of 5° with the fcc directions (red line) and a shift δ indicating a bcc (110) stacking (image size 3.7 nm × 3.7 nm). **c,** Identification of the two phases as ferromagnetic bcc and antiferromagnetic fcc by their LDOS: typical normalized differential conductance spectrum (continuous lines) on the island rim (orange) and in the island centre (blue), compared to the calculated spin-averaged LDOS of 2 ML Fe/Cu(111) in the ferromagnetic bcc and antiferromagnetic fcc configurations (dashed lines).
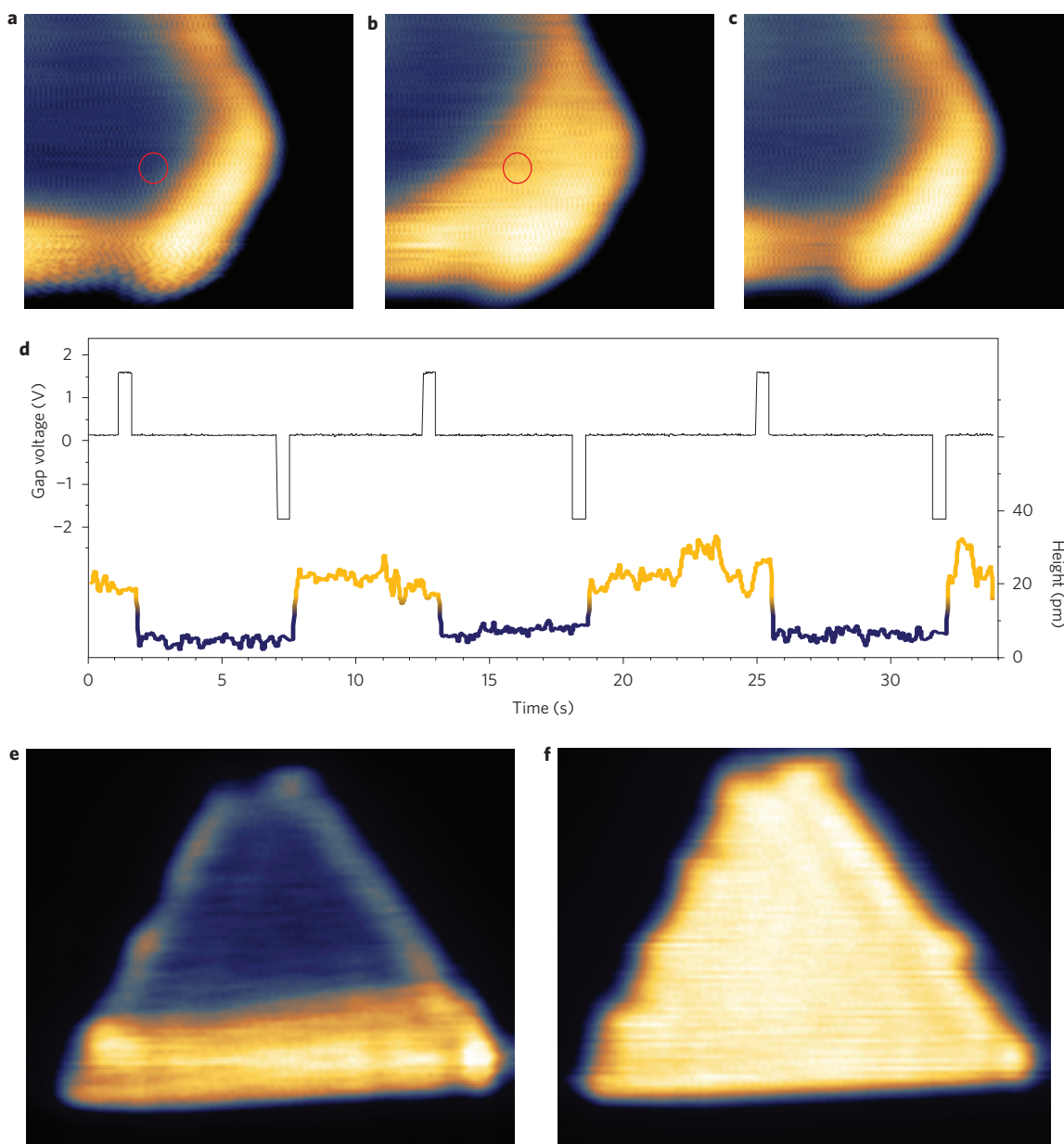
Figure 3 | Controlled switching with electric fields. a–c, Switching of antiferromagnetic fcc (blue) and ferromagnetic bcc (orange) areas with electric field pulses. Three STM scans of an island corner were recorded at subcritical electric fields. By applying a positive field pulse after the acquisition of scan **a**, the bcc region is expanded in **b** and reduced again by a negative field pulse in **c**. Image sizes in **a–c**, 6 nm × 6 nm. Positions of the pulses are marked in red. **d**, Applied gap voltage (black line) and height (coloured line) recorded as function of time at a fixed tip position. It can be seen that the switching process is deterministic and reproducible. **e,f**, Small Fe islands can be completely switched from an antiferromagnetic fcc (**e**) to a ferromagnetic bcc (**f**) structure. Image size in **e** and **f**, 11 nm × 9 nm (horizontal × vertical).

by also varying the lateral displacement of the Fe atoms in the presence of the electric field. The layers were relaxed along the vertical direction as a function of the lateral displacement, resulting in the total energy of the layers for ferromagnetic and antiferromagnetic configurations. Our simulations demonstrate that, under a positive field, the ferromagnetic bcc stacking is unstable and fcc stacking with layerwise antiferromagnetic order of the two Fe layers is energetically most favourable (Fig. 1c). Additionally, there is an energy barrier of 20 meV at a displacement of 0.25 Å for the transformation to the fcc state. In the case of a negative applied electric field (Fig. 1d), the expanded fcc stacking is ferromagnetically ordered and unstable, and can transform to the energetically favoured ferromagnetic bcc structure (for more details on the energy landscape, see Supplementary Information).

Structure and magnetism in iron islands

To confirm these predictions experimentally, we performed STM measurements at 4.3 K in ultrahigh vacuum on Fe layers deposited by molecular beam epitaxy at 300 K onto clean Cu(111) surfaces. Fe/Cu(111) is known to nucleate in two atomic-layer high triangular islands[15], as illustrated in the STM image in Fig. 2a. The triangular islands, however, display an inhomogeneous structure. Two different coexisting phases of Fe can be distinguished as different apparent heights (Fig. 2a). Recently, Biedermann and colleagues showed in atomically resolved STM studies that the islands consist of fcc Fe in the centre, and the rim has a bcc structure[15]. In atomically resolved STM images (Fig. 2b), we identified the same crystallographic phases. In the centre, the atoms show a perfect hexagonal order with the lattice directions and distances of the fcc Cu substrate
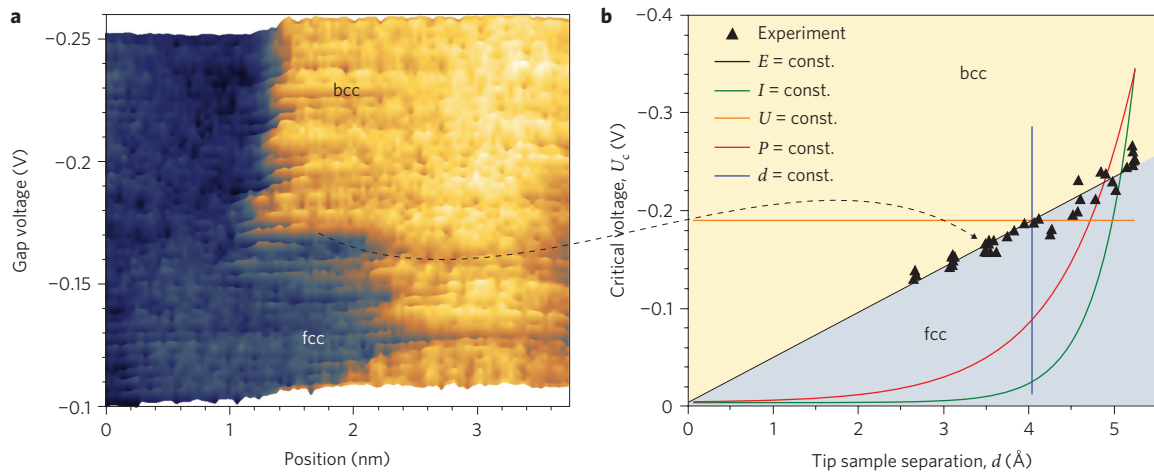
Figure 4 | Controlling fcc versus bcc structures with the local electric field. a, A single line across the fcc–bcc domain boundary was scanned with the STM, decreasing the gap voltage scan line by scan line. At a critical gap voltage (0.16 V) a transition from fcc to bcc occurs. This experiment has been carried out at different tunnelling currents (in a range from 150 pA to 28 nA), that is, with different tip sample separations. **b**, By plotting the critical gap voltage against the corresponding tip–sample separation, the boundary (black triangles) in the phase diagram is obtained. The experimental results can be compared with possible distance dependencies of the critical voltage (coloured lines) resulting from different models (E, constant electric field; I, constant current; U, constant voltage; P, constant power; d, constant distance; for details see main text). The curves are all fitted freely to the experimental data.

(red grid). At the rims, however, two directions of the bcc structure (green) deviate by small angles from the fcc substrate direction (red), and the third is aligned with the fcc lattice (red) but with a small shift to the bridge positions of the bottom Fe layer (δ). In agreement with the work by Biedermann and colleagues[15], this indicates a Kurdjumov–Sachs orientation of the bcc structure.

To verify the predicted magnetic configuration of the two phases, we performed spin-polarized STM and scanning tunnelling spectroscopy (STS) measurements on the centre and rim of the islands. The spin-polarized STM experiments on the bcc and fcc regions showed no lateral magnetic superstructures within the phases, excluding rowwise antiferromagnetic, triple-q or 120° Néel spin structures in both fcc and bcc phases. To distinguish the remaining ferromagnetic and layerwise antiferromagnetic configurations, STS experiments were performed. The measured differential conductance dI/dU normalized by the tunnelling matrix element T is to first order proportional to the local density of states (LDOS) according to an extended Tersoff–Hamann approach[16,17] (for details see Methods). These experimental spectra were used as electronic fingerprints to identify the magnetic state by comparison with the LDOS of different magnetic phases of fcc and bcc Fe layers calculated by a first-principles Green function method especially designed for layered semi-infinite systems[18]. The LDOS in the STM geometry was calculated at a tip height of ~4 Å above the surface layer, mirroring the STM experiment.

The experimental spectrum of the island rim matches well with the theoretical LDOS of a ferromagnetic bcc structure (Fig. 2c), and the spectrum of the island centre agrees well with the LDOS of a layerwise antiferromagnetic fcc Fe. The LDOS of other magnetic configurations did not match the experimental observations at all (see Supplementary Information). In particular, the peak close to the Fermi energy in the fcc spectrum can only be explained by an antiferromagnetic order. Its position depends strongly on the interlayer distance of Fe. The best agreement between experimental and theoretical data is obtained at an interlayer distance between the two Fe layers of 2.00 Å for fcc Fe and 2.12 Å for bcc Fe (Fig. 2c). This height difference is also found in the STM images (cf. Fig. 2a). The STS measurements, in combination with atomically resolved images, have confirmed the fcc/bcc structures and revealed the magnetic order of the two coexisting phases. Thus, in the following we identify them by their apparent height in the topographic STM image (blue for antiferromagnetic fcc and orange for ferromagnetic bcc). The clear distinction of the two states offers the opportunity to read out the magnetic state.

Switching the magnetic order by local electric fields
Following the theoretical predictions, we applied electric field pulses in the tunnelling junction with the tip positioned close to the domain boundary between the fcc and bcc areas. An enlarged view of an Fe island is shown in Fig. 3a, with fcc and bcc areas recorded at low electric fields. A field pulse of $+5.5 \times 10^9$ V m^{-1} and of 50 ms duration was applied with the STM, leading to an expansion of the bcc area laterally by about 1 nm (Fig. 3b). This configuration was stable at 4.3 K until a second pulse of -5.5×10^9 V m^{-1} was applied, switching the area back to an fcc structure (Fig. 3c). This phase transition is mainly observed near the fcc–bcc domain boundary. However, islands smaller than 10 nm could be completely switched from a dominantly antiferromagnetic fcc (Fig. 3e) to a fully ferromagnetic bcc structure (Fig. 3f). We experimentally ruled out that the switching was driven by adsorption-induced effects such as structural modifications because of hydrogen contamination (see Supplementary Information), and have confirmed using STS that when the crystal structure is switched, the electronic structure also switches accordingly. This experimentally verified the capability to induce a crystallographic and magnetic transition. Furthermore, the stability of both phases at a low electric field confirms the above predicted barrier between fcc and bcc configurations. This switching process is deterministic and reproducible, as can be seen in Fig. 3d. By applying alternating field pulses (black line), the magnetic phase could be switched back and forth (coloured line). Switching could be achieved by pulses as short as 60 μs, the time limit of our STM set-up (see Supplementary Information). These experiments illustrate that, with an STM, information can be written, stored and read out on the nanometre scale.

In the calculations only electric fields were applied. In our experiments, however, tunnelling currents were also present, and an overlap of the wavefunctions of tip and sample is significant. To verify MEC as the switching mechanism we carried out a systematic study of the phase transition. The basic experiment comprised scanning along a single line across the domain boundary many times, varying the tunnelling parameters. First, the gap voltage U was decreased line by line from −0.10 V to −0.25 V with the tunnelling

current I kept constant. Figure 4a shows the arrangement of fcc and bcc as function of the gap voltage plotted in the y direction. It was found that at a critical value of the gap voltage U_c (0.16 V in Fig. 4a), a transition from fcc to bcc occurs, shifting the domain boundary to the left. This gives us a value of U_c for a chosen I. Determination of the critical voltage was then repeated at different tip sample distances d, scanning exactly the same line on the sample. This was achieved by varying the tunnelling current. Finally, we obtained a set of points describing the relation between critical voltage U_c and distance d. As the distance was *a priori* unknown, it was determined from the experimental current distance relation (for details see Supplementary Information). The electric field in the STM junction was given by the gap voltage over d. Figure 4b plots the critical voltage U_c against distance d. In other words, this figure provides the phase diagram. Above the critical voltage the bcc phase is preferred and below it, the fcc phase is favoured. In the interval from 3 to 6 Å a linear distance dependence of the critical voltage was found; in particular, a freely fitted straight line passes through the origin. Thus, the boundary in the phase diagram corresponds to a constant electric field, in agreement with a magnetic phase transition by means of MEC, verifying the theoretical predictions. A series of experiments with different tips and Fe islands revealed critical electric fields in the range between 3×10^8 and 9×10^8 V m^{-1}, in good agreement with calculations. These fields are close to those used in recent experiments on MEC[19].

To test further for mechanisms not related to MEC, the experimental data were compared with relations resulting from different scenarios (Fig. 4b). The transition could be directly caused by the current, for example, due to spin torque[20], spin accumulation[21] or electromigration. This would lead to a switching that only depends on the tunnelling current (I = const., green line). This, however, disagrees with the observed dependence. Similarly, mechanisms that relate to the energy of the tunnelling electrons (such as inelastic excitation of specific lattice vibrations or electronic excitations; U_c = const., yellow line) or local heating (population of a continuum of excited vibronic or electronic states, $P = I \cdot U_c$ = const., red line) do not fit the experimental data. Mechanical forces between the tip and the sample due to the overlap of their wavefunctions[22] (d = const., blue line) also fail to explain the data. Indeed, this excludes these other switching mechanisms.

Conclusions

Because the studied phase transition in Fe is of first order (activated) and is reversible, it confirms a prototype for writing, storing and reading information on the nanometre scale. The dream of storing information magnetically and switching it electrically is thus not restricted to the class of insulating materials, but has been proven to be valid at metallic surfaces as well. The observed effect is not a peculiarity of Fe, because the underlying structural and magnetic phase transition occurs in a whole variety of transition metals.

Methods

Relaxations with an applied electric field. To simulate atomic relaxations in Fe/Cu(111), the Vienna *Ab initio* Simulation Package (VASP)[14,23,24] was used within the generalized gradient approximation (GGA-PBE) approximation[25] for exchange and correlation effects. Electron–ion interactions were described by the projector-augmented wave (PAW) pseudopotential[26], and the electronic wavefunctions were represented by plane waves with a cutoff energy of 600 eV. To model the (111) surface of Cu, we constructed a 7 ML (monolayer) thick (~1.5-nm) supercell, with a vacuum spacer of 2 nm. The in-plane fcc lattice parameter was set to the experimental value of 2.5561 Å. The two top Cu monolayers and two Fe adlayers in this asymmetric slab were relaxed. For ionic relaxations the $12 \times 12 \times 4$ k-point Monkhorst–Pack[27] mesh was used. Ionic relaxation was performed within the spin-polarized mode, starting from the ferromagnetic or, alternatively, from the antiferromagnetic configuration in the Fe layers, until the forces were less than 7×10^{-3} eV/Å. To calculate the electronic charge density as well as the local magnetic moments, we used the tetrahedron method with a k-mesh of $32 \times 32 \times 16$ points for each completely relaxed atomic configuration. To imitate the presence of an external electric field in our numerical simulations we used a plate capacitor placed in

vacuum at a distance ~4–5 Å above the surface[28]. The plates of the capacitor were separated by a vacuum spacer to avoid interaction and charge transfer between them. Thus, one plate of the capacitor placed above the Fe adlayers simulates either a negatively or positively charged tip. The strength of the electric field was chosen to be 10^9 V m^{-1}. Non-equilibrium effects were not taken into account in the model.

Simulations of STM spectra. To simulate scanning tunnelling spectra we used the Tersoff–Hamann treatment for the tunnelling current[16]. In this approximation, the tunnelling current is proportional to the LDOS of the surface at the tip position. In the present work the LDOS was calculated from first principles using a Green function multiple-scattering approach[29] within density functional theory in the local spin density approximation (LSDA). The method was specially designed for layered systems by treating adequately semi-infinite boundary conditions[30]. The LDOS for the Fe/Cu(111) system was calculated from non-spherical potentials determined self-consistently for bulk, surface and vacuum regions.

Experimental set-up. The STM tips were chemically etched from a tungsten wire and cleaned in a vacuum chamber by melting the end of the tip. The Cu(111) substrate was prepared by sputtering with 3 keV Ar$^+$ ions followed by annealing to 450 °C to obtain a clean and flat surface. About 0.2 ML of pure Fe were deposited by molecular beam epitaxy at a substrate temperature of 300 K. Both this preparation and our studies in the STM were carried out in ultrahigh vacuum ($p < 1 \times 10^{-10}$ mbar). The differential conductance dI/dU was obtained with a lock-in technique using a sinusoidal modulation of 5 mV and a frequency of 16.4 kHz. When ramping the voltage, the feedback loop was open. As the experimental dI/dU spectra not only depend on the LDOS but also on the tunnelling probability T, they cannot be compared directly with a calculated LDOS. We therefore normalized our spectra using the tunnelling probability T: $LDOS \propto dI/dU \cdot 1/T$. As shown by Ukraintsev[17] this allows a deconvolution of density of states and tunnelling probability within a WKB (Wentzel Kramers Brillouin) approach. The applied gap voltage is defined as the potential of the tip with respect to the sample.

References

1. Smolenskii, G. A. & Chups, I. E. Ferroelectromagnetism. *Soviet Physics Uspekhi* **25,** 475–493 (1982).
2. Lottermoser, T. *et al.* Magnetic phase control by an electric field. *Nature* **430,** 541–544 (2004).
3. Spaldin, N. A. & Fiebig, M. The renaissance of magnetoelectric multiferroics. *Science* **309,** 391–392 (2005).
4. Zheng, H. *et al.* Multiferroic BaTiO$_3$–CoFe$_2$O$_4$ nanostructures. *Science* **303,** 661–663 (2004).
5. Zavaliche, F. *et al.* Electric field-induced magnetization switching in epitaxial columnar nanostructures. *Nano Lett.* **5,** 1793–1796 (2005).
6. Duan, C.-G., Jaswal, S. S. & Tsymbal, E. Y. Predicted magnetoelectric effect in Fe/BaTiO$_3$ multilayers: ferroelectric control of magnetism. *Phys. Rev. Lett.* **97,** 047201 (2006).
7. Fechner, M. *et al.* Magnetic phase transition in two-phase multiferroics predicted from first principles. *Phys. Rev. B* **78,** 212406 (2008).
8. Lang, N. D. & Kohn, W. Theory of metal surfaces: charge density and surface energy. *Phys. Rev. B* **1,** 4555–4568 (1970).
9. Weisheit, M. *et al.* Electric field-induced modification of magnetism in thin-film ferromagnets. *Science* **315,** 349–351 (2007).
10. Weissmüller, J. *et al.* Charge-induced reversible strain in a metal. *Science* **300,** 312–315 (2003).
11. Moruzzi, V. L., Marcus, P. M., Schwarz, K. & Mohn, P. Ferromagnetic phases of bcc and fcc Fe, Co, and Ni. *Phys. Rev. B* **34,** 1784–1791 (1986).
12. Bain, E. C. The nature of martensite. *Trans. Am. Inst. Min. Metall. Pet. Eng.* **70,** 25–46 (1924).
13. Sandoval, L., Urbassek, H. M. & Entel, P. The Bain versus Nishiyama–Wassermann path in the martensitic transformation of Fe. *New J. Phys.* **11,** 103027 (2009).
14. Kresse, G. & Furthmüller, J. Efficiency of ab-initio total energy calculations for metals and semiconductors using a plane-wave basis set. *Comput. Mater. Sci.* **6,** 15–50 (1996).
15. Biedermann, A., Rupp, W., Schmid, M. & Varga, P. Coexistence of fcc- and bcc-like crystal structures in ultrathin Fe films grown on Cu(111). *Phys. Rev. B* **73,** 165418 (2006).
16. Tersoff, J. & Hamann, D. R. Theory and application for the scanning tunneling microscope. *Phys. Rev. Lett.* **50,** 1998–2001 (1983).
17. Ukraintsev, V. A. Data evaluation technique for electron-tunneling spectroscopy. *Phys. Rev. B* **53,** 11176–11185 (1996).
18. Lüders, M., Ernst, A., Temmerman, W. M., Szotek, Z. & Durham, P. J. Ab initio angle-resolved photoemission in multiple-scattering formulation. *J. Phys. Condens. Matter* **13,** 8587–8606 (2001).
19. Maruyama, T. *et al.* Large voltage-induced magnetic anisotropy change in a few atomic layers of iron. *Nature Nanotech.* **4,** 158–161 (2009).

20. Slonczewski, J. C. Conductance and exchange coupling of two ferromagnets separated by a tunneling barrier. *Phys. Rev. B* **39,** 6995–7002 (1989).
21. Jedema, F. J., Filip, A. T. & van Wees, B. J. Electrical spin injection and accumulation at room temperature in an all-metal mesoscopic spin valve. *Nature* **410,** 345–348 (2001).
22. Hofer, W. A., Fisher, A. J., Wolkow, R. A. & Grütter, P. Surface relaxations, current enhancements, and absolute distances in high resolution scanning tunneling microscopy. *Phys. Rev. Lett.* **87,** 236104 (2001).
23. Kresse, G. & Hafner, J. Ab initio molecular-dynamics simulation of the liquid–metal–amorphous-semiconductor transition in germanium. *Phys. Rev. B* **49,** 14251–14269 (1994).
24. Hafner, J. Ab-initio simulations of materials using VASP: density-functional theory and beyond. *J. Comput. Chem.* **29,** 2044–2078 (2008).
25. Perdew, J. P., Burke, K. & Ernzerhof, M. Generalized gradient approximation made simple. *Phys. Rev. Lett.* **77,** 3865–3868 (1996).
26. Kresse, G. & Joubert, D. From ultrasoft pseudopotentials to the projector augmented-wave method. *Phys. Rev. B* **59,** 1758–1775 (1999).
27. Monkhorst, H. J. & Pack, J. D. Special points for Brillouin-zone integrations. *Phys. Rev. B* **13,** 5188–5192 (1976).
28. Neugebauer, J. & Scheffler, M. Adsorbate–substrate and adsorbate–adsorbate interactions of Na and K adlayers on Al(111). *Phys. Rev. B* **46,** 16067–16080 (1992).
29. Lüders, M., Ernst, A., Temmerman, W. M., Szotek, Z. & Durham, P. J. Ab initio angle-resolved photoemission in multiple-scattering formulation. *J. Physics Condens. Matter* **13,** 8587–8606 (2001).
30. Szunyogh, L., Újfalussy, B., Weinberger, P. & Kollár, J. Self-consistent localized KKR scheme for surfaces and interfaces. *Phys. Rev. B* **49,** 2721–2729 (1994).

Author contributions

L.G., T.K.Y. and W.W. conceived and designed the experiments. L.G., T.B., A.F.T. and R.J.H.W. performed the experiments. L.G., R.J.H.W. and T.K.Y. analysed the data. A.E., I.M. and S.O. designed the calculations. A.E., S.O. and M.D. performed the calculations. M.F. and M.D. contributed analysis tools. A.E., L.G., I.M. and W.W. co-wrote the paper. All authors discussed the results and commented on the manuscript.

Additional information

The authors declare no competing financial interests. Supplementary information accompanies this paper at www.nature.com/naturenanotechnology. Reprints and permission information is available online at http://npg.nature.com/reprintsandpermissions/. Correspondence and requests for materials should be addressed to W.W.